

# A mechanism for coastal fog genesis at evening transition

Thomas J. Hintz<sup>1</sup>  | Kelly Y. Huang<sup>1</sup> | Sebastian W. Hoch<sup>2</sup> | Stef L. Bardoel<sup>3</sup>  |  
Saša Gaberšek<sup>4</sup>  | Ismail Gultepe<sup>5</sup> | Jesus Ruiz-Plancarte<sup>6</sup> | Eric R. Pardyjak<sup>7</sup> |  
Qing Wang<sup>5</sup> | Harindra J. S. Fernando<sup>1</sup>

<sup>1</sup>Aerospace and Mechanical Engineering Department, University of Notre Dame, Notre Dame, Indiana, USA

<sup>2</sup>Atmospheric Sciences Department, University of Utah, Salt Lake City, Utah, USA

<sup>3</sup>Civil and Environmental Engineering and Earth Sciences Department, University of Notre Dame, Notre Dame, Indiana, USA

<sup>4</sup>US Naval Research Laboratory—Marine Meteorology Division, Monterey, California, USA

<sup>5</sup>Engineering and Applied Sciences, Ontario Tech University, Oshawa, Ontario, Canada

<sup>6</sup>Meteorology, Naval Postgraduate School, Monterey, California, USA

<sup>7</sup>Department of Mechanical Engineering, University of Utah, Salt Lake City, Utah, USA

## Correspondence

Thomas J. Hintz and Harindra J. S. Fernando, Aerospace and Mechanical Engineering Department, University of Notre Dame, Notre Dame, IN 46556, USA.  
Email: [thintz1@nd.edu](mailto:thintz1@nd.edu) and [hfernand@nd.edu](mailto:hfernand@nd.edu)

## Funding information

Office of Naval Research, Grant/Award Number: N00014-21-1-2296

## Abstract

Transitional changes in the atmospheric boundary layer (ABL) are known to facilitate the onset of terrestrial fog, which is defined as a condition with near-surface visibility <1 km due to airborne water droplets. In particular, the evening transition from a daytime convective ABL to a night-time stable ABL provides favorable conditions for fog. This article describes a local fog event observed during the evening transition at a Canadian islet in the north Atlantic known as Sable Island during the “Fog and Turbulence Interactions in the Marine Atmosphere (Fatima)” field campaign. The comprehensive set of data collected using a myriad of instruments covering a wide range of scales allowed identification of a novel mechanism underlying this fog event. Therein an ocean–land discontinuity created a flow regime consisting of several stacked boundary layers, interplay of which produced a thin low-level cloud that then diffused downward to the surface, causing visibility reduction. This mechanism offers useful insights on the role of boundary layers, stratification, and turbulence in fog genesis over oceanic islands.

## KEY WORDS

fog, evening transition, boundary layer, entrainment, low-level clouds

## 1 | INTRODUCTION

Fog is defined as a near-surface collection of suspended water droplets or ice crystals that causes horizontal visibility to drop below 1 km where relative humidity is

near 100% (WMO, 2014, 2017). The surface layer of the atmospheric boundary layer (ABL) profoundly affects the formation, evolution, and dissipation (i.e., life cycle) of fog, thus causing the dynamics and thermodynamics of fog to be fundamentally more complex and different from those

of clouds, although knowledge derived from cloud micro-physics has been valuable in fog research and forecasting.

Fog causes logistical and safety issues across an array of human activities. Reduction in visibility leads to dangerous conditions when traveling, be it by land, air, or sea (Gultepe *et al.*, 2007; Johnson & Graschel, 1992; Koračin *et al.*, 2014; Mazon *et al.*, 2018; Snowden *et al.*, 1998). In urban settings, fog entraps dangerous pollutants when water vapor condenses onto particulate matter to create smog (Barwick *et al.*, 2019).<sup>1</sup> Fog severely affects free-space optical communications technologies that use light propagation in the atmosphere to transmit data for telecommunications, computer networks, and even drone guidance. High-energy laser (directed-energy) defense systems have become popular because of their effectiveness in asymmetric warfare, for which optical scattering and molecular absorption and scattering from fog constitute a hindrance (Fiorino *et al.*, 2020; Kaymak *et al.*, 2018; Perram *et al.*, 2010). Knowledge of fog physics is also critical for better understanding of ecological processes, viticulture, and extraction of potable water from fog amidst global water crises and the looming threat of climate change (Klemm *et al.*, 2012; Weathers, 1999).

Various classifications exist to characterize fog depending on the formation mechanism and location, based on which three broad categories of fog can be identified: radiation, advection, and mixing fog (Fernando *et al.*, 2021). Nocturnal radiative cooling of a moist air layer to or below its dew point  $T_{\text{dew}}$  leads to radiative fog. Advection of warmer air over colder ocean leads to cold sea fog, the converse of which is warm sea fog, both belonging to the general category of advection fog. Nonlinear mixing of nearly saturated warm and colder air masses produces mixing fog (Taylor, 1917). Other classifications include, for example, steam fog (steam streaks/smoke arising within cold fog), precipitation fog (rain evaporating near saturation), ice fog (small ice crystals forming at air temperatures  $T < -10^{\circ}\text{C}$ : (Gultepe *et al.*, 2015)), and location-based fogs such as marine fog, valley fog, upslope fog, and land fog (Gultepe *et al.*, 2007). The term “marine fog” encompasses coastal fog in the coastal zone, sea fog that forms over shallower “green” water away from the coastal zone, such as in marginal seas (e.g., Yellow Sea) and continental shelves (e.g., Grand Banks), and open-ocean fog that forms over deeper “blue” water, as discussed by (Koračin *et al.*, 2014) and (Koračin & Dorman, 2017). Marine environments, being rich in moisture and aerosols, are favorable for fog, with airborne salt from sea spray, bioaerosols, and advected continental aerosols acting as fog condensation nuclei (Woodcock, 1978).

Environments supportive of fog formation are typically moist, with clear nights and light winds. Additionally, it is acknowledged that an extremely complex mix of factors,

including profiles of temperature  $T$  (stratification), relative humidity  $RH$ , wind speed and direction, turbulence, radiative flux divergence, topographic effects, surface conditions (roughness, moisture, soil properties), and aerosol composition and loading all contribute to the fog life cycle (Fitzjarrald & Lala, 1989; Maurer *et al.*, 2019). On a fundamental level, three processes are identified as essential for fog; cooling, moistening, and vertical mixing of air parcels with different  $T$  and  $RH$  (Duynkerke, 1991), which contribute in different proportions under different conditions.

In the evening, rapid reduction of incoming shortwave (SW) radiation while the net longwave (LW) radiation remains negative leads to a reversal of the sign of net radiation  $Q_{\text{net}}$ , which in turn causes rapid cooling of a thin air layer (thickness  $<50$  cm) near the ground by conduction, causing a sharp temperature gradient (Blay-Carreras *et al.*, 2015). Overlying turbulent eddies generated during the cooling process penetrate and carry cooler air upward to develop a turbulent layer ( $\sim 1$  m thickness) undergoing cooling at a rate of several  $\text{K}\cdot\text{hr}^{-1}$  (Turton & Brown, 1987). Gradual vertical turbulent diffusion of colder air from this layer leads to a stable boundary layer (SBL), which grows slowly because of inhibition of turbulence by stable stratification. The period of SW radiation reduction preceding the switching of a convective boundary layer (CBL) to an SBL is the evening transition, which, on flat terrain, is accompanied by a reduction of turbulence, although turbulence does not quench fully in the SBL because of surface shear production (Lothon *et al.*, 2014; Nadeau *et al.*, 2011). (Fitzjarrald & Lala, 1989) demonstrated that the transition from CBL to SBL causes moisture convergence near the ground, and the accompanying increase of  $RH$  augmented by cooling is a simple mechanism of fog generation. They acknowledged, however, that a myriad of other processes such as horizontal moisture advection in river valleys and coastal areas may also contribute to fog formation.

The above-mentioned mechanism is more applicable to radiative fog over land, given nocturnal cooling of land-surface air is stronger than that of marine-surface air because of high thermal capacity and nocturnal convection in the upper ocean. Other fog-gensis mechanisms over open ocean include advection of warm moist air over negative sea-surface temperature (SST) gradients. For example, in the Grand Banks area in the North Atlantic, southwesterly flow passes over warm Gulf Stream waters toward the colder Labrador Current, producing cold sea fog. Analogously, colder air from the north above the Labrador Current may intrude southward to produce warm sea fog. Consequently, the Grand Banks has the world’s highest (observable) summer fog frequency, with peak fog occurrence of 45% during the months of June, July, and August (Dorman *et al.*, 2017). This led to the conduction of the first field campaign of the “Fog

and Turbulence Interactions in the Marine Atmosphere (Fatima)" project during July 1–31, 2022 in the area covering the Grand Banks (GB) and the regions of Sable Island and Hibernia Oil Platform.

A previous study by (Fernando *et al.*, 2021) noted other fog formation mechanisms present in this area, for example, mixing fog in the coastal areas of Newfoundland (Bardoel *et al.*, 2021; Wang *et al.*, 2021). This article reports yet another marine fog-genesis mechanism identified during the Fatima–GB campaign during the observations at Sable Island on July 21. It involves interaction between the internal boundary layer (IBL) and the marine convective boundary layer (MCBL) during the evening transition over Sable Island. Observations show the appearance of a low-level (~30–50 m) thin stratus cloud during the rapid cooling period of evening transition due to IBL and MCBL interactions, and top-down diffusement of "cloud puffs" into the surface layer to reduce visibility (*Vis*), fluctuating at first >1 km, then decreasing and remaining <1 km, with the surface layer filling up with saturated air to form a thick fog layer.

Section 2 of the article describes the observational site and relevant instrument placement on Sable Island, followed by data analysis in Section 3. Detailed analysis of the fog event in point is described in Section 4, based on which a hypothesis for a novel fog formation mechanism is developed and presented in Section 5. Discussion and conclusions are given in Section 6.

## 2 | HIGHLIGHTS OF FATIMA–GB FIELD CAMPAIGN

### 2.1 | Observation site

The Fatima Grand Banks (Fatima–GB) campaign was conducted during July 1–31, 2022, off the coast of eastern Canada, with observational platforms being a research vessel (R/V *Atlantic Condor*), Sable Island (SI), and the Hibernia oil platform. The first two were instrumented mainly by Fatima PIs and collaborators, while routine monitoring data from the Hibernia platform was accessed through Wood Plc. Inc. The ship trekked in the Grand Banks area north of Sable Island as well as south of the island on a north–south (N–S) transect from the Gulf Stream to Sable Island. Several wave gliders were deployed to support air–sea interaction studies.

This article concerns land-based observations on Sable Island (43.9337°N, 59.9149°W), a small island in the Atlantic Ocean about 300 km southeast of Halifax, Nova Scotia, chosen due to its location across a N–S oceanic temperature gradient and frequently advecting fog past it. SI has a low topography (maximum elevation of just 30 m),

a slender, curved shape (1.3 km wide at its widest point, 40 km long), and is devoid of tall vegetation (vegetation consists only of grass, reaching up to ~1 m in height). It is uniquely positioned for measuring maritime fog passing southwest (SW) to northeast (NE), disturbed by the islet. The island experienced fog (visibility < 1 km) for ~25% of the total time of the experiment. Figure 1 includes a map of the island's location, as well as the layout of the main instrumentation areas.

On the western part of the island, in an area dubbed "West Light", four main measurement clusters were set up with comprehensive instrumentation, including three meteorological towers labeled North Tower, Center Tower, and South Tower, as well as a fourth area labeled Micro-physics Tower. The three meteorological towers (North, Center, and South) were placed in a row, aligned in the predominant S/SW climatological wind direction to observe evolution of fog over the island. Owing to Sable Island's status as a Canadian National Park Reserve, all scientific operations required stringent considerations of ecological conservation approved via an Environmental Impact Report. Instruments were deployed in park-approved areas of little to no protected vegetation so as to not damage the limited food sources of the island's natural inhabitants. All instruments were placed within electric fence enclosures to ensure the safety of the equipment as well as the 569 horses living on the island at that time. Existing structures such as fence posts and concrete pads were utilized in instrumentation deployment, park-provided generators served as the power source for all equipment, and the research team lodged in an existing house in the West Light area.

### 2.2 | Instrumentation: Center tower

The bulk of instrumentation used in this study was located in the center tower area. On the tower itself, instruments were positioned at heights of 2, 5, 8, and 13 m above ground level to provide a vertical profile of various measurements (Figure 2).

RM Young-81000<sup>®</sup> sonic anemometers located at 5, 8, and 13 m provided three-dimensional easternly, southerly, and vertical wind speeds (*U*, *V*, *W* respectively) at a sampling rate of 20 Hz. A Campbell Scientific IRGASON<sup>®</sup> located at 2 m provided three-dimensional wind speed as well as water-vapor mixing ratio (*r*) and barometric air pressure (*p*) at a sampling rate of 40 Hz. Vaisala HMP-155 probes at 2, 5, 8, and 13 m provided temperature (*T*) and relative humidity (*RH*) values at a sampling rate of 1 Hz.

Located 20 m west of the center tower was a Vaisala Forward Scatter Sensor FD70<sup>®</sup> (Figure 2) to measure visibility. Visibility is used as a proxy for fog intensity and



**FIGURE 1** Left: map showing the location of Sable Island off the east coast of Canada. Map data from ArcGIS. Right: layout of main instrumentation areas in the West Light region on Sable Island. [Colour figure can be viewed at [wileyonlinelibrary.com](http://wileyonlinelibrary.com)]



**FIGURE 2** Photo of the center tower, labeled with heights of instrumentation (left), radiation-measurement sawhorse (center), and FD70 enhanced present weather detector (right). [Colour figure can be viewed at [wileyonlinelibrary.com](http://wileyonlinelibrary.com)]

is inversely proportional to liquid water content (Gultepe *et al.*, 2017). Data were captured every 15 seconds at a height of 2.5 m above ground level.

Located ~5 m east of the center tower was a radiation and soil measurement area (Figure 2). For radiation measurements, a sawhorse structure was fitted with two pyranometers and two pyrgeometers to measure shortwave and longwave radiation, respectively. One pyranometer and one pyrgeometer pointed upwards, at 1.8 m above ground to measure incoming radiation, while the others pointed downwards to measure outgoing radiation, at a height of roughly 1.4 m above ground level. For the evaluation of the soil energy budget, two soil heat-flux plates were buried 5 cm beneath the surface of the ground, and a temperature-averaging probe sampled soil temperature between 0 and 5 cm depth.

Located ~30 m NE of the center tower was the rawinsonde launch site. Vaisala MW41<sup>®</sup> rawinsondes were used to measure vertical profiles of  $T$ ,  $RH$ ,  $p$ , and  $U$  up

to several km. Launches occurred regularly throughout the campaign at 0000 and 1200 UTC, and far more frequently (every 1 or 3 hours) during intensive operational periods (IOPs), which were enacted when fog events were forecast. Throughout the month of July, 14 IOPs were called, each ranging from 3 to 48 hours in duration, though typically lasting around 30 hours. All IOPs triggered equipment; however, they did not always run continuously, due to weather and labor requirements or hardware sensitivity.

### 2.3 | Instrumentation: Microphysics tower

The microphysics tower area was located approximately 50 m west of the center tower, and, of the numerous commercial pieces of equipment located there, a Vaisala CL-51<sup>®</sup> ceilometer and a DMT FM-120<sup>®</sup> fog monitor were

used for this study (Figure 3). The CL-51 was situated at ground level (measurement apparatus at 1 m) and was used to measure aerosol backscatter and determine cloud-base height and, more importantly for this study, the presence of suspended droplets (fog) near the surface. The FM-120 was situated approximately 1 m above the ground level and was used to measure the number concentration of fog droplets present in air near the surface ( $N_d$ ). Both systems operated continuously throughout the experiment.

Also located in the vicinity of the microphysics tower was a novel in-house built instrument dubbed the super combo probe, an instrument that utilizes a probe array of both cold wires and hot films to measure fine-scale velocities and temperatures. Built upon previous similar instruments that were dubbed the combo probe (Goldshmid

*et al.*, 2022; Kit *et al.*, 2010), this iteration features several mechanical design reconsiderations as well as the addition of nanowire sensors to the probe array. For this study, the super combo probe was used to measure TKE dissipation rate  $\bar{\epsilon}$  and temperature variance dissipation rate  $\bar{\chi}_T$ . Additional information on the super combo probe as well as photos (Figure S1) can be found in the Supplementary Material.

A summary of the instrumentation utilized for this article can be found below in Table 1, and a comprehensive description of instrumentation will be given in an article to be submitted to the Bulletin of the American Meteorological Society (Fernando *et al.* 2024).

### 3 | DATA ANALYSIS

This study is focused on an interesting fog event that occurred on the evening of July 21, 2022, within the Intensive Operational Period IOP #9. The time frame of emphasis is the six-hour window 1800–0000 UTC (1500–2100 LT).

The wind speed, wind direction,  $T$ , and  $RH$  acquired from the center tower instrumentation were all processed as 5-minute averages. Averaging was done to ensure an accurate portrayal of mean values by avoiding the finest-scale fluctuations, which could potentially worsen the signal-to-noise ratio. Longer, commonly used averaging periods, such as 15 minutes, were avoided because of the transitory nature of fog, which requires effective capturing of the finer-scale fluctuations representative of fog evolution encapsulated within synoptic trends, particularly during the evening transition, when environmental conditions change significantly within 15-minute windows. The sonic anemometer located at a height of 5 m was experiencing technical difficulties in this the



FIGURE 3 Photo of CL-51 and FM-120 deployment in the microphysics tower area. GCIP pictured to the left of the FM-120, not used in analysis. [Colour figure can be viewed at [wileyonlinelibrary.com](http://wileyonlinelibrary.com)]

TABLE 1 Instrumentation summary.

Instrument	Location	Height (m)	Parameters measured
RM Young 81000 sonic anemometer	Center Tower	5, 8, 13	$U, V, W$
CS IRGASON	Center Tower	2	$U, V, W, r, p$
Vaisala HMP-155	Center Tower	2, 5, 8, 13	$T, RH$
Vaisala FD70	20 m W of Center Tower	2.5	$Vis$
Kipp and Zonen CMP21 Pyranometer	Radiation/soil	1.8 in, 1.4 out	SW radiation
Kipp and Zonen CGR4 Pyrgeometer	Radiation/soil	1.8 in, 1.4 out	LW radiation
Hukseflux HFP01SC Soil heat-flux plate	Radiation/soil	−0.05	$Q_{gr}$
CS TCAV Soil temp. probe	Radiation/soil	−0.05 to 0	$T_s$
Vaisala MW41 rawinsondes	30 m NE of Center Tower	0 to 5000	$T, RH, p, U$
Vaisala CL-51	Microphysics Tower	1	Aerosol backscatter
FM-120	Microphysics Tower	1	$N_d$

period of emphasis, so its dataset was excluded from the analysis.

Backscatter data from the CL-51 were processed every 15 seconds, and an estimate of the ABL height was made by following the work of Münkel and Roininen (2010), which is based on a significant decrease in backscatter occurring at the ABL height.

Using both pyranometers and pyrgeometers, net radiation was quantified by adding both longwave and shortwave incoming radiation, then subtracting both forms of outgoing radiation. Soil temperature and ground heat flux ( $Q_{\text{gr}}$ ) were output directly by the soil temperature probe and ground heat-flux plate, respectively.

The turbulent sensible heat flux  $Q_s$  and the vertical water-vapor flux  $Q_{\text{wr}} = \overline{w'r'}$  were calculated using the IRGASON-measured temperature flux  $\overline{w'T'}$  ( $w'$  being the vertical velocity fluctuations,  $T'$  being the temperature fluctuations) and water-vapor mixing ratio fluctuation  $r'$  at 2 m, respectively, on the center tower (Large & Pond, 1982). The overbar denotes 5-minute averages.

The turbulent buoyancy flux  $g\alpha\overline{T'_v w'}$ , with  $\alpha$  being the thermal expansivity and  $T_v$  the absolute virtual temperature, was used to calculate the convective velocity  $w_* = (\overline{g\alpha T'_v w' h})^{1/3}$  pertinent to a convective boundary layer, where  $h$  is the boundary-layer height Kaimal *et al.* (1976). The buoyancy gradient (squared Brunt–Väisälä frequency) was calculated using

$$N^2 = \frac{g}{\theta_v} \frac{\partial \theta_v}{\partial z},$$

where  $g$  is gravity and  $\theta_v$  is the virtual potential temperature. The stability of the turbulent shear flow under stable conditions is indicated using the gradient Richardson number, which was calculated using

$$Ri_g = \left[ \frac{g}{\theta} \frac{\partial \theta_v}{\partial z} \right] / \left[ \left( \frac{\partial U}{\partial z} \right)^2 + \left( \frac{\partial V}{\partial z} \right)^2 \right]$$

(Hanna, 1969). Another stability indicator used was the Monin–Obukhov (length) scale,

$$L = \frac{-u_*^3 T_v}{\kappa g Q_v},$$

$\kappa$  being the von Karman constant ( $\kappa=0.41$ ) and  $u_* = \left[ \left( \overline{u'w'} \right)^2 + \left( \overline{v'w'} \right)^2 \right]^{1/4}$  the friction velocity based on Reynolds stresses. The production of turbulence by shear was calculated as

$$S = - \left( \overline{u'w'} \frac{dU}{dz} + \overline{v'w'} \frac{dV}{dz} \right),$$

with measurements based on  $z = 2$  m and  $z = 13$  levels.

## 4 | FOG EVENT AND MEASUREMENTS

### 4.1 | Event overview

The event in point occurred on July 21, 2022, during IOP 9, where fog gradually formed on Sable Island during the evening transition over a period of 90 minutes. Water droplets appeared at the ground level, first with a slight decrease in visibility at 2035 UTC (1730 local time, LT), and fluctuating visibility thereafter, and fog was considered to be fully formed once near-surface visibility dropped below 1 km at 2200 UTC (1900 LT) (Figure 4).

The period 1800 UTC, July 21 to 0000 UTC, July 22 was selected for study for several reasons. One is data availability, as the majority of the expansive instrumentation array was collecting data without malfunctions. Another is the interest of studying fog formation during evening transition, in a backdrop of completely clear skies with  $>10$  km visibility throughout the morning and afternoon before seeing dramatic changes during the switch from a convective regime to a stable boundary layer. GOES-East visible satellite images showed no high-level clouds in the area during the fog formation period, and brightness temperature difference (BTD) images therein indicated ground-level moisture advection into the area. The third reason is the intriguing observation that fog is being formed locally on Sable Island, rather than advecting from the south to SI as commonly observed on the island. The visible (camera) images in Figure 5 show that a thin layer of low-level cloud (LLC), similar to stratus clouds, forms at a height  $\sim 30$ –50 m (estimated from the height of the lighthouse in Figure 5). There are no signatures of convective (cumulus) activity, updrafts, or lifting of surface air, as evident from the low vertical turbulent intensities in the

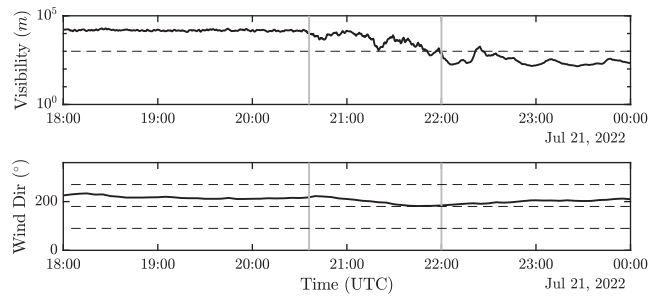


**FIGURE 4** Time series of visibility and wind direction. The dashed horizontal line in the top plot represents the 1-km visibility threshold of fog definition. The dashed horizontal lines in the bottom plot represent cardinal directions: 90° as east, 180° as south, 270° as west, and 0/360° as north. The vertical gray lines represent the start and end of the gradual fog formation period (visibility drop from  $>10$  km to 1 km) and will be present in subsequent figures to serve as a visual aid relating various plots. (Local time LT = UTC – 3 hours.)



**FIGURE 5** Photos from Sable Island during the fog event on July 21, labeled with the time each photo was taken. These were captured from a camera on the south tower pointing NE. The lighthouse seen in each photo is 25 m tall and  $\sim$ 200 m from the camera. (LT = UTC – 3 hours.) [Colour figure can be viewed at [wileyonlinelibrary.com](http://wileyonlinelibrary.com)]

surface layer (see later, Figure 11). Within about half an hour, this LLC diffuse down and fills the air layer near the surface (i.e., top-down diffusion). A timelapse (Video S1) is available as Supplementary Material taken from a camera located on the south tower pointing north (inland), supporting the above observations further.

Ceilometer aerosol backscatter profiles from each of the main instrumentation areas (north, center, and south) also indicate that this is not an advection event, as the north area actually shows the earliest LLC and fog formation, notwithstanding that the wind flow is southwesterly (Figure 6). There is no accessible evidence on whether or not fog had formed over the ocean simultaneously, but what is observed here is sufficient to show distinctly that this event can be considered local rather than an advection fog occurrence. The surface-level moisture layer arriving on SI from the southwest indicated by GOES-East BTD images is consistent with ceilometer backscatter data (cyan color) prior to fog genesis. The formation of fog at a significant height from the ground and diffusing down was intriguing, and its coincidence with the evening transition period is curious.

As mentioned in Section 1, numerous classifications exist for fog, and an early classification by (Byers *et al.*, 1951), revised by Tardif and Rasmussen (2007), identified the following types: precipitation fog, radiation fog, advection fog, fog resulting from cloud-base lowering,

and morning evaporation fog. The fog event described above was closest to the “cloud-base lowering fog”, defined as gradual lowering of the cloud base over a few hours, eventually to osculate the ground surface. There was a difference, however, that rather than gradual lowering of the cloud base, following the appearance of the stratus, there was entrainment from its base and puffs of clouds diffused downward and filled the lower layer within 5–10 minutes, which is consistent with the time for air parcels to descend from the cloud-base height  $h_B$  to the ground  $\approx h_B/(0.3\sigma_w) \approx (50 \text{ m})/[0.3 \times (0.5–0.25) \text{ m}\cdot\text{s}^{-1}] \approx 5–10$  minutes (Fernando, 1988), where  $\sigma_w$  is the characteristic root-mean-square (rms) vertical velocity in the surface layer (Figure 11). This is evident from Figure 6, where hints of LLC appear (yellow) in ceilometer backscatter at  $\sim 2000$  UTC, LLC backscatter becomes stronger (red color) at  $\sim 2020$ , and cloudy air puffs due to entrainment appear at the surface at 2035, simultaneous with visibility fluctuations. Fog with  $Vis < 1 \text{ km}$  appears at 2200 (Figure 4, Table 2).

## 4.2 | Timeline

Table 2 identifies interesting and useful transition points. Sometimes, sunset (item 11 in the table) is used as the onset of evening transition, but, as pointed out by Kaimal *et al.* (1976), the sensible heat flux  $Q_s$  that drives buoyant convection is shut off about 1–2 hours before the sunset

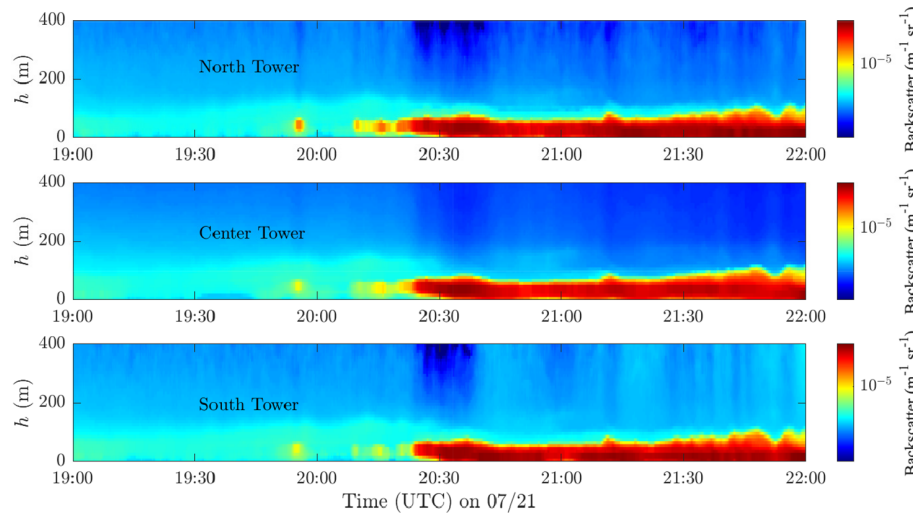


**FIGURE 6** Time series of aerosol backscatter from ceilometers located at the north, center, and south tower areas. [Colour figure can be viewed at [wileyonlinelibrary.com](http://wileyonlinelibrary.com)]

**TABLE 2** Chronological details of data observations during the evening of July 21. Time is in UTC (LT = UTC – 3 hours).

Time	Event	#
2020	Initial $T$ decrease	(1)
	Collapse of MCBL	(2)
2035	$Q_{\text{gr}} \approx 0$	(3)
	Initial droplet appearance/visibility reduction	(4)
2040	Initial TKE decrease	(5)
2135	$Q_S \approx 0$ at $z = 13$ m	(6)
2200	Fog appearance	(7)
2230	$N^2$ sign flip	(8)
2300	$Q_{\text{net}} \approx 0$ at $z = 2$ m	(9)
2330	$Q_S \approx 0$ at $z = 2$ m	(10)
2336	Sunset	(11)

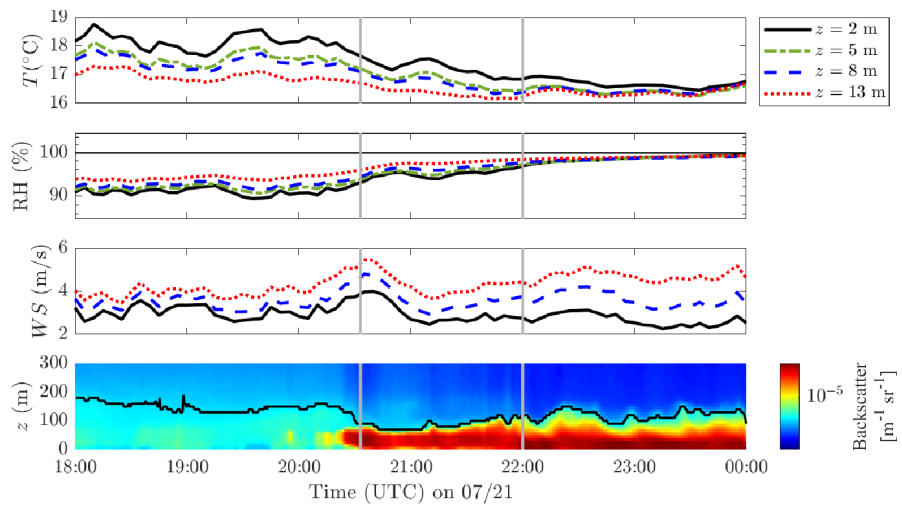
(6), making sunset an unsuitable dynamical indicator for transition, which is also the case here. Other indicators could be the zero crossing of the net radiation  $Q_{\text{net}}$  (9), as well as the net ground heat flux  $Q_{\text{gr}}$  (3) and the surface-air temperature difference, which remained positive during the period of inspection in our case. Other dynamic indicators of transition could be the initiation of the rapid decrease of  $T$  (1) or TKE (5) near the surface, the collapse of the MCBL (2), as evident from the backscatter of the CL-51 ceilometer, change of sign of the buoyancy gradient  $N^2$  near the surface (8), and onset of visibility reduction (4). Measurements and methods involved in developing the table, as well as in producing parameters shown in the following section, appear in the Supplementary Material.

#### 4.3 | General parameters/background flow

Figure 7 shows the time series of visibility (replotted), mean longitudinal wind speed (WS), temperature, relative humidity, and ceilometer CL-51 backscatter.

The temporal changes thereof are driven by the diurnal cycle; the general reduction of  $T$ , fluxes, and turbulent kinetic energy TKE, and, to some extent, the increase of RH are all related to the evening reduction of incoming solar radiation. Nonetheless, some curious features are embedded within such trends, which are related to fog genesis at 2200 UTC following a period of slow surface visibility reduction starting at 2035 UTC. A noteworthy observation is the steep temperature decrease near the surface

**FIGURE 7** Time series of  $T$ ,  $RH$ ,  $WS$ , and aerosol backscatter from the center tower. The black line in the aerosol backscatter plot represents the estimated atmospheric boundary-layer height. Vertical gray lines correspond to those in Figure 4 and indicate times that bound the fog formation process. ( $LT = UTC - 3$  hours.) [Colour figure can be viewed at [wileyonlinelibrary.com](http://wileyonlinelibrary.com)]



starting from 2020 UTC, coinciding with a distinct upward trend of  $RH$  at lower levels, with relative humidity  $RH$  increasing from  $\sim 90\%$  toward saturation, assuming  $> 95\%$  at 2200 UTC and saturation at 2300 UTC.

The rapid decrease of  $T$  was also associated with rising wind speed that peaks  $\sim 2035$  UTC, which could be associated with an increase of near-surface stability expressed in terms of squared Brunt–Väisälä frequency  $N^2$  or the gradient Richardson number  $Ri_g$  (discussed later), causing damping of turbulence and increase of winds (discussed later, under Figure 11). It is interesting that the gradual reduction of visibility started at the wind-speed peak (2035 UTC) with a reduction of turbulence levels.

Note the CL-51 backscatter measured up to approximately 175 m initially before 2035 UTC, which can be interpreted as the height of the MCBL with aerosols passing over SI until the visibility reduction begins. This is marked by the black line representing atmospheric boundary-layer height  $h$  evaluated using the strongest vertical backscatter gradient. There is then a sudden reduction of  $h$  below 100 m, an indication of collapse of turbulence within the MCBL. As low-level cloud forms, the top of the MCBL can no longer be seen, due to signal attenuation by droplets, which prevents the ceilometer beam from penetrating past the high backscatter.

Although CL-51 resolution near the surface is rather coarse ( $\approx 10$  m), the backscatter shows air becoming increasingly droplet-laden at  $\sim 2000$  UTC between 25 and 75 m first (yellow coloration). The droplet concentration then increases (red) and quick top-down diffusion of droplets (red) then occurs, to hug the ground around 2035 UTC. Further evolution of the near-surface layer leads to fog formation at 2200 UTC, evident from the highest backscatter levels near the ground (dark red) in the lowest 20 m, consistent with visibility data ( $< 1$  km) and photographs in Figure 5.

#### 4.4 | Cooling at the evening transition

To investigate the details of cooling at the evening transition, Figure 8 depicts how the soil and air temperature, ground heat flux, and net radiation decay, and how vertical fluxes and stability parameters respond to waning radiative forcing into the evening.

The soil temperature stays significantly higher than the air temperature throughout the evening transition (Figure 8a), but the ground's heat flux  $Q_{gr}$  decreases and crosses zero at 2035 (Figure 8b), coincident with the drop in visibility first seen. This indicates that, while the environment never reaches a point where the surface is cooler than the air, there is a significant reduction in soil temperature and thermal shift in the surface seen in  $Q_{gr}$  as the net radiation decays to zero throughout the evening transition. The decay of soil temperature, zero-crossing of ground heat flux, and decay of net radiation (Figure 8c) are clear causes for the reduction of near-surface temperature and sensible heat flux, leading to a change from a strongly convective to an increasingly stable boundary layer. Interestingly, compared with a normal day, the net radiation reversal is damped due to the presence of the LLC and fog, which provide increased incoming longwave radiation, reducing the radiative cooling rate of the near-surface air layer.

The result is apparent from the four lower plots (Figure 8d–g), as vertical fluxes  $Q_s$  and  $Q_{wr}$  as well as stability parameters  $Ri_g$  and  $N^2$  all trend towards zero in step with net radiation throughout the evening. In all, the above four parameters decrease in magnitude in the 20 minutes leading up to the first visibility drop at 2035 UTC. This is also followed by a steady decay of parameters throughout the fog formation process, ultimately approaching zero directly at or immediately following the full formation of fog ( $Vis < 1$  km) at 2200 UTC. It is evident that the

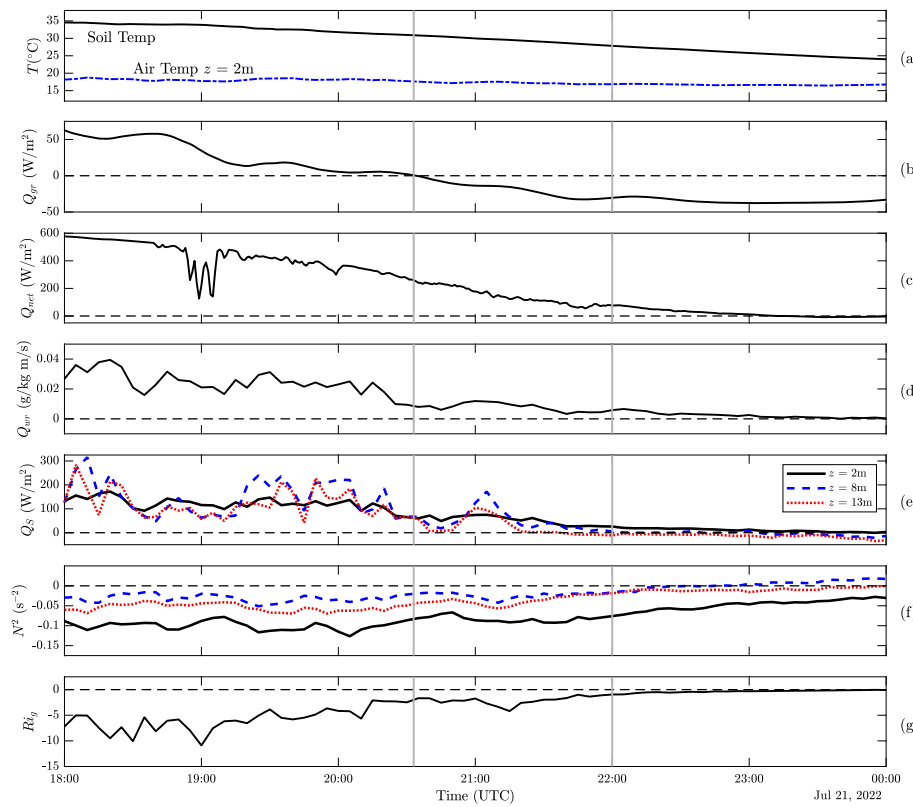


**FIGURE 8** Time series of (a) soil and 2-m air temperature  $T_s$  and  $T$ , respectively, (b) ground heat flux  $Q_{gr}$ , (c) net radiation  $Q_{net}$  at  $\sim 1.5\text{ m}$ , (d) water-vapor flux  $Q_{wr}$  at  $2\text{ m}$ , (e) sensible heat flux  $Q_s$ , (f) squared Brunt–Väisälä frequency  $N^2$ , and (g) Richardson gradient number  $Rig$  between  $2$  and  $13\text{ m}$ .  $Q_{gr}$  is positive when directed away from the surface (downward into the soil). Vertical gray lines correspond to those in Figure 4 and indicate times that bound the fog formation process. (LT = UTC – 3 hours.) [Colour figure can be viewed at [wileyonlinelibrary.com](http://wileyonlinelibrary.com)]

cooling of air near the surface is due to net radiation reduction during the evening transition, and subsequently the demise of convection, as exhibited by the turbulent kinetic energy measurements to be discussed later. The environment responds to cooling with collapsing vertical fluxes and becomes both dynamically and statically stable (Figure 8d–g).

#### 4.5 | Upper layer and MCBL

Figure 9 shows rawinsonde profiles from three launches at 1800, 2100, and 2359 UTC to observe the behavior of the atmosphere at higher altitudes.

Three distinct layers could be identified in the profiles: an IBL developing over SI that undercuts the MCBL, and an outer stratified layer. The convective IBL (negative temperature gradient) reaches up to roughly  $30\text{ m}$ , the MCBL reaches up to  $\sim 180\text{ m}$ , the capping thermally stratified layer sits above it all, and a stable interfacial layer (IL) sits in the  $30\text{--}70\text{ m}$  range. These layers are indicated in a schematic that is used to describe the appearance of the LLC and fog later in Figure 13. The region immediately above the IL shows a well-mixed layer, which is possibly the remnant MCBL that extends up to  $\sim 200\text{ m}$  at 1800 UTC followed by a collapse to  $\sim 160\text{ m}$  at 2100 UTC.

The wind velocity increases in the lowest  $200\text{ m}$  during 1800–2100, and after the evening transition a

jet forms in the MCBL with velocity peaking at  $125\text{ m}$ , giving rise to strong wind shear in the lower  $250\text{ m}$  of the atmosphere, particularly near the surface. The relative humidity increases over time as expected, the peak being at an altitude of  $\sim 60\text{ m}$ , within the IL. The composition of profiles is in agreement with the notion of fog forming  $\sim 40\text{--}60\text{ m}$  above the surface, where the temperature is close to a minimum and relative humidity is near its maximum in the two profiles before 2200 UTC.

The temperature profiles remain approximately similar over time at higher levels, but in the lowest  $30\text{ m}$  there is noticeable intense cooling, approaching near-stable conditions by the 2359 UTC profile. A steeper temperature gradient can be seen forming at height  $30\text{--}60\text{ m}$  in the IL, where condensation appears at 2000–2030 UTC (Figure 7), and this region has undergone slight heating by the 2359 UTC radiosonde, perhaps due to latent heat release. The region immediately above the IL shows a well-mixed layer, which is the remnant MCBL that extends up to  $\sim 200\text{ m}$  at 1800 UTC followed by a collapse to  $\sim 160\text{ m}$  at 2100 UTC. The increase of its depth thereafter may be due to mixing by turbulence generated from enhanced shear at such heights.

Figure 10 shows how scales of turbulence carrying the sensible heat flux  $Q_s$  evolve with time, in the form of their spectra. Before 2035 UTC, the heat-flux spectrum shows activity at larger scales with roughly two peaks. The first (i) comes from overturning eddies of convection over

**FIGURE 9** Vertical profiles of temperature, relative humidity, and wind speed from rawinsonde launches. Horizontal gray bars represent altitudes where boundaries between the observed layers are roughly present throughout the evening transition. (LT = UTC – 3 hours.) [Colour figure can be viewed at [wileyonlinelibrary.com](http://wileyonlinelibrary.com)]

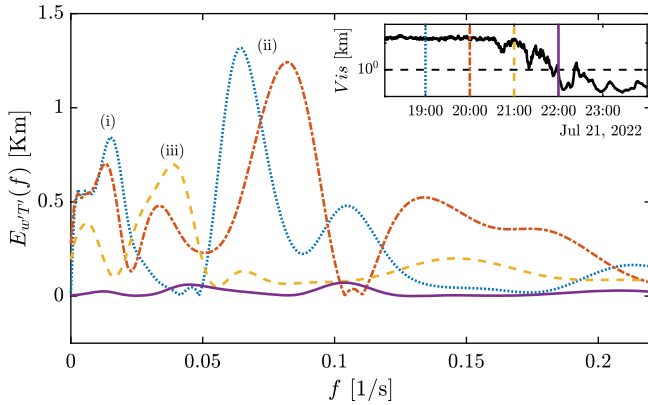
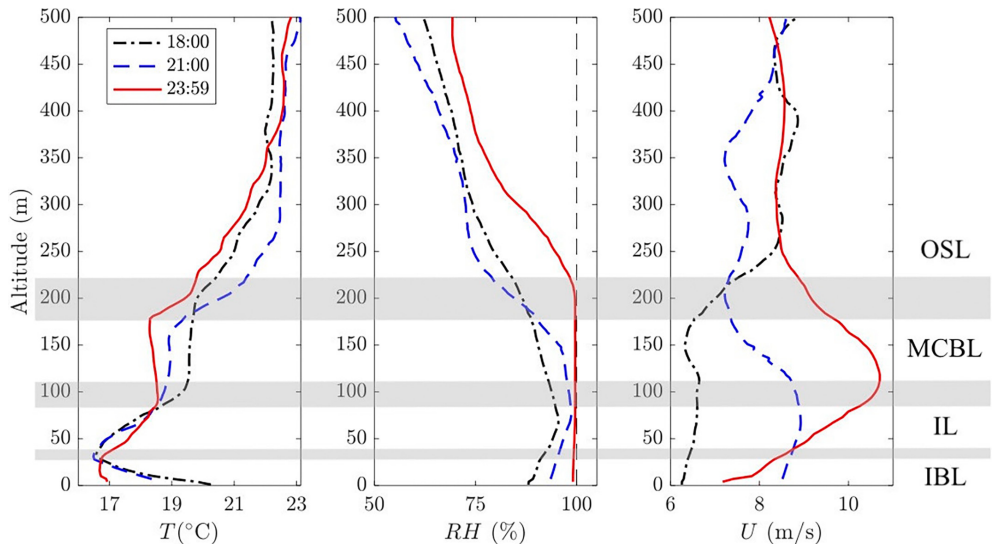


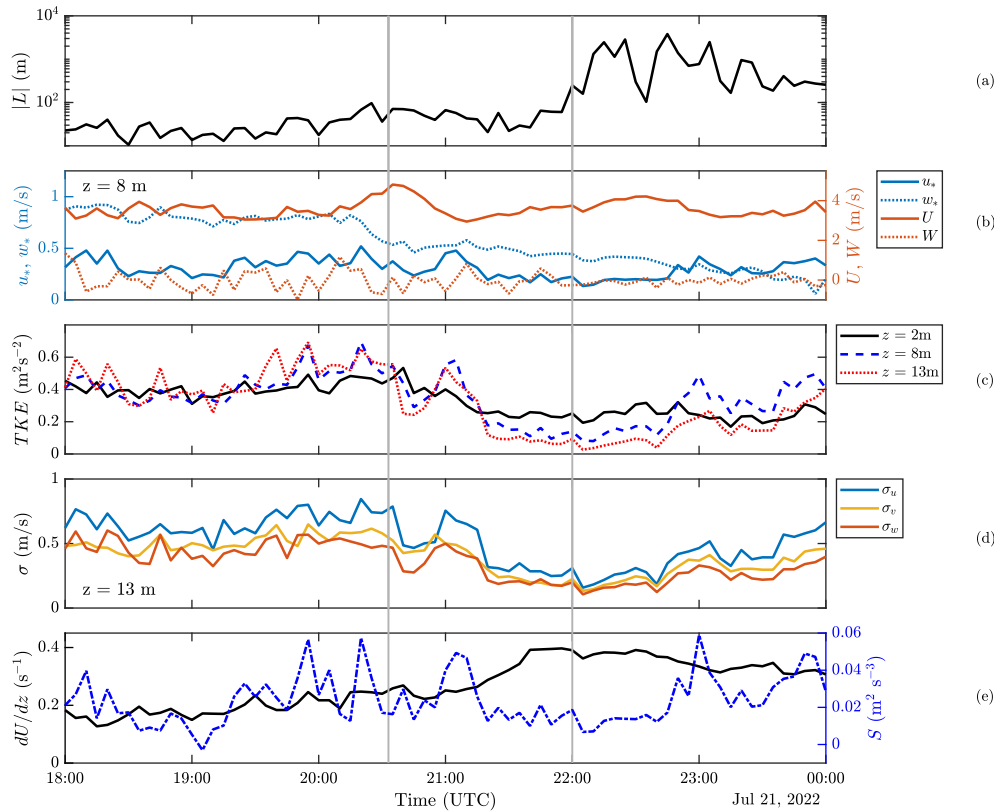
**FIGURE 10** Power spectra of the kinematic vertical sensible heat flux at a height of 13 m. The colored vertical lines in the visibility plots coincide with the colored lines representing the power cospectra. (LT = UTC – 3 hours.) [Colour figure can be viewed at [wileyonlinelibrary.com](http://wileyonlinelibrary.com)]

the entire depth  $h \approx 200$  m, the frequency of  $\sigma/(0.25)h \sim 0.7/(0.25 \times 200) \sim 0.01$  Hz, carrying a substantial portion of heat flux. The second peak (ii) is from eddies generated within the IBL shear layer of depth  $h_L \approx 40$  m with a frequency of  $\sigma/(0.25)h_L \sim 0.7/(0.25 \times 40) \sim 0.07$  Hz, which contributes to the upward transport of the surface heat flux ( $\sigma$  values are from Figure 11, to be discussed next). These estimates agree well with the spectra of Figure 10 for times 1900 and 2000 UTC. At 2100, the IL appears to decouple the IBL and MCBL, and the eddies in the lower layer are expected to have a single dominant frequency (iii) corresponding to a layer depth of 40 m, that is,  $\sigma/(0.25)h_L \sim 0.45/(0.25 \times 40) \sim 0.045$  Hz.  $Q_s \approx 0$  at 2135 UTC (Table 2), and thus its cospectrum collapses to vanishing values from then onward.

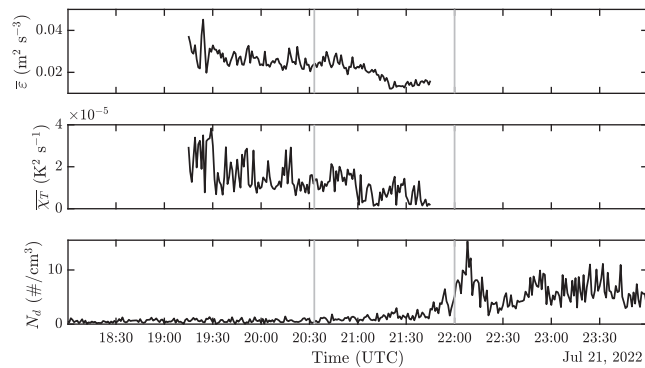
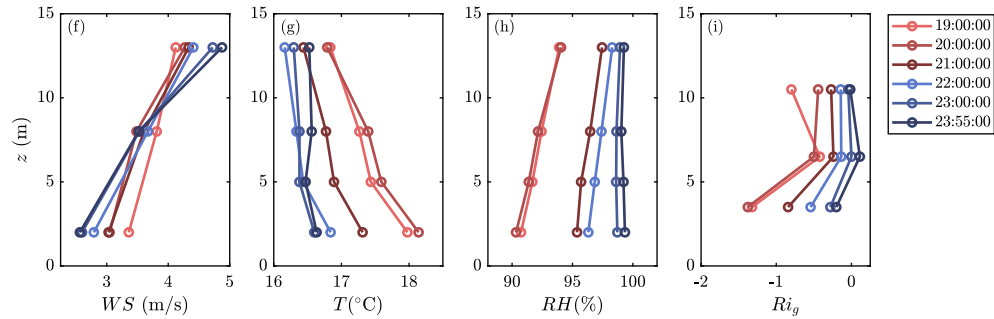
#### 4.6 | IBL and turbulent mixing

Figure 11 directs attention back near the surface to explore the turbulence and temporal development of vertical profiles within the IBL, showing salient physical and dynamical quantities based on central flux tower measurements during convective, near-neutral, and stable conditions, together with the Monin–Obukhov length-scale (Figure 11a). These include friction, convective and mean velocities,  $TKE$ , rms velocities, vertical shear (based on the lowest two levels of the flux tower), vertical mean shear, and shear production of turbulence.

Note the steeper decay of  $TKE$  occurring from around 2035 UTC until about 2200 UTC when  $Q_s \approx 0$ . The modulations of  $TKE$ , rms velocities and shear production are interesting (Figure 11c,d,e), with low values during fog genesis, slowly increasing while fog conditions prevail toward midnight, while friction velocity (Figure 11b) is seen steadily declining, in line with the vertical fluxes seen in Figure 8.  $RH$  remains high throughout the near-surface vertical profile (Figure 11h), with humidity levels being higher at greater heights before the entire near-surface region experiences full saturation. The tendency toward the development of stable stratification near the ground (Figure 11g) dampens the vertical transfer of momentum, hence leading to an increase of shear (Figure 11f), which, in turn, leads to (intermittent) turbulence production. In this case, the gradient Richardson number  $Ri_g$  remains negative throughout the period shown (Figure 11i), and hence turbulence production is due purely to shear instabilities. In the case where distinct stable stratification develops ( $Ri_g > 0$ ), turbulence occurs when  $Ri_g$  drops below a critical value (Pardyjak *et al.*, 2002). The plots within Figure 11 also show that, while decreasing during



**FIGURE 11** (a) Time series of  $L$ , friction velocity  $u_*$ , and convective velocity  $w_*$ , as well as (b) mean flows  $U$  and  $W$  at 8 m, (c)  $TKE$ , (d) rms velocities  $\sigma$  at 13 m, (e) wind shear  $dU/dz$  and shear production of turbulence  $S$  at 8 m, and near-surface vertical profiles of (f) wind speed  $WS$ , (g)  $T$ , (h)  $RH$ , and (i)  $Rig$ . Vertical gray lines correspond to those in Figure 4 and indicate times of significance to the fog formation process. ( $LT = UTC - 3$  hours.) [Colour figure can be viewed at [wileyonlinelibrary.com](http://wileyonlinelibrary.com)]



**FIGURE 12** Time series of  $TKE$  dissipation rate  $\bar{\epsilon}$ , temperature variation dissipation rate  $\bar{X}_T$ , and droplet number concentration  $N_d$ .  $\bar{\epsilon}$  and  $\bar{X}_T$  were measured with the super combo at  $z = 3$  m, and  $N_d$  with FM-120 at  $z \approx 1$  m. Vertical gray lines correspond to those in Figure 4 and indicate times that bound the fog formation process. ( $LT = UTC - 3$  hours.)

the evening transition, turbulence is still present to mix fog down to the surface from the IL until full saturation is reached after 2200 UTC.

The decreasing turbulence level is also seen in the high-resolution measurements of the super combo probe located at a height of 3 m (Figure 12). The super combo measures the dissipation of  $TKE$  and scalar ( $T$ ) fluctuations with very high resolution within clear and light fog conditions. Owing to the sensitivity of the probes for suspended water droplets, the super combo was deployed for a limited duration before fog set in. The  $TKE$  dissipation rate  $\bar{\epsilon}$  exhibits a noticeable decay around 2130 UTC to approximately half of its value at 2035 UTC. The temperature variance dissipation rate  $\bar{X}_T$  similarly exhibits a decrease around 2130. These reductions are analogous to the reduction in  $TKE$  (Figure 11) and reflect the increasing stability of the IBL, which eventually led to the collapse of the kinematic vertical heat flux (Figure 10). Although

the sensitivity of the probes precludes data throughout the entirety of the fog genesis, both  $\bar{\varepsilon}$  and  $\bar{x_T}$  appear to stabilize after approximately 2130 and 2100, respectively. This suggests that turbulence is still present and could serve to entrain water droplets that have formed at the interface between the IBL and MCBL down to the surface. The droplet number concentration  $N_d$  near the surface increases significantly beginning shortly after 2130, supporting the notion that top-down entrainment carries low-level cloud droplets toward the surface, filling up the air layer up to the IL.

## 5 | FOG FORMATION MECHANISM

Careful inspection of observations and measurements in Section 4 led us to propose an interesting fog formation mechanism schematized in Figure 13. This proposal follows iterations of several hypotheses that were refined to describe the observations best.

During the day (Figure 13a), the IBL is strongly convective (unstable) with a near-surface negative temperature gradient due to land heating, and the overlying MCBL is mostly mixed, with turbulence advected from the ocean as well as mechanical and convective turbulence penetrating from the IBL below. The curious temperature structure due to disparity of temperatures between the MCBL and the upper part of the convective IBL results in a stable inversion layer (IL) at the top of the IBL. This IL evolves spatially, initially weak in stability with eddies of both layers penetrating freely in and out of it in the daytime, crossing between the IBL and MCBL. The stratification below the IL is unstable, the IL itself is weakly stable, and the advected MCBL above is quasi-homogeneous. Both the IBL and MCBL encounter high levels of relative humidity sourced from the marine environment, providing a moist, favorable environment for fog (Figure 9).

The main shift into the evening transition is the rapid cooling of the land surface when the soil temperature decreases as net (in-out) radiation approaches zero.

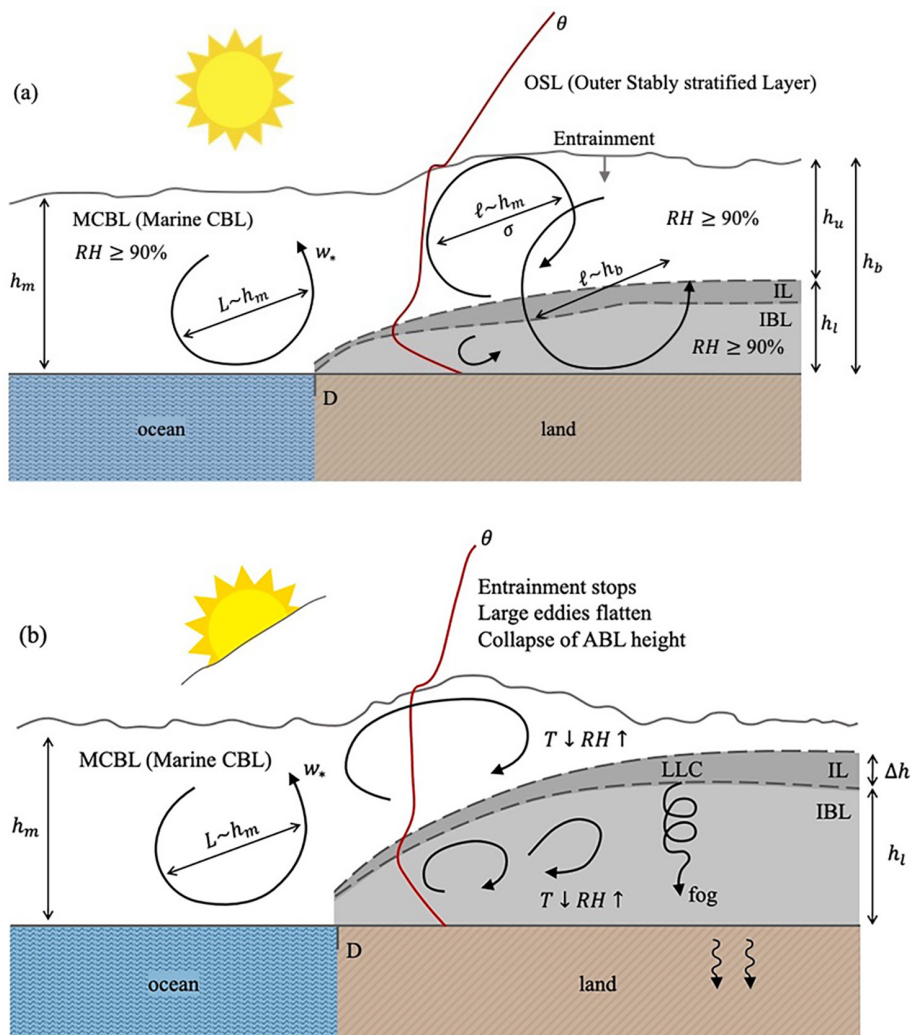


FIGURE 13 Diagrams of the boundary-layer flow during both (a) daytime (time ~1800 UTC) and (b) the evening transition (time ~2100 UTC). [Colour figure can be viewed at [wileyonlinelibrary.com](http://wileyonlinelibrary.com)]

Strong temperature changes are seen closest to the surface due to changes of the radiation budget, so cooling within the IBL is significantly stronger than cooling within the MCBL overhead. The rapidly decreasing temperature in the IBL compared with the slowly decreasing temperature in the MCBL causes the IL to become increasingly stable. With (slow) oceanic cooling, increased IL stability, and weaker MCBL capacity to entrain from the outer stably stratified layer, eddies in the MCBL become feeble, while turbulence is sustained in the IBL as a result of stronger near-surface wind shear.

With evening transition progressing, the stability of the IL increases to the point where turbulence in the MCBL collapses completely, resulting in anisotropic, elongated eddies that can no longer overturn (Hannoun, 1987). Can be found online at <https://thesis.library.caltech.edu/854/>; Fernando & Hunt, 1997). As the eddies in the MCBL stop overturning, the entrainment of lower *RH* air occurring at the interface of the MCBL and outer stratified layer stops. This phenomenon of entrainment inhibition during the evening transition and collapse of large-scale eddies has been observed previously at the upper level of penetrating CBLs, but in the context of evening transition onset over land (Caughey & Kaimal, 1977; Caughey & Palmer, 1979). This condition is shown in Figure 13b, wherein there exists no substantial entrainment into the MCBL, no substantial eddy penetration into the IL from the MCBL and IBL, and a weakly turbulent IL, with some entrainment from the IL into the IBL possible due to ground-shear-induced turbulence at the lower surface of the IL (Strang & Fernando, 2001). Shear across the IL is too weak to break up the IL, thus it mostly survives during the evening transition.

Decreasing temperatures of both the MCBL and IBL cause *RH* to increase in both layers, with mixing between the two layers abated by the stratified IL, yet local mixing across the IL is still possible (Fernando, 1991). That is, mixing of colder high-*RH* air from the IBL and somewhat warmer high-*RH* air from the collapsing MCBL may lead to saturated water vapor or droplets at the IL through the mixing fog formation mechanism proposed by (Taylor, 1917). These droplets are confined to the IL, and hence their appearance takes the form of a LLC, which is clearly seen in the photographs in Figure 5. After fog has formed at the interface (IL) of the IBL and MCBL, continued downward entrainment by IBL turbulence transports saturated air from the LLC toward the ground, leading to visibility reduction near the surface, identified as fog by instrumentation. This fog persists into the night as vertical fluxes wane with the completion of evening transition. High saturation levels and low temperatures (which continue to decrease with the cooling of the land's

surface) provide favorable conditions for continued fog until a mechanism of fog dissolution comes into play.

## 6 | DISCUSSION AND CONCLUSION

The first field campaign of the Fatima project was conducted in the Grand Banks area, off the coast of eastern Canada, during July 1–31, 2022. A comprehensive suite of instruments was deployed on three platforms: Sable Island, a research vessel (*R/V Atlantic Condor*), and the Hibernia oil platform. Daily weather forecasting based on Coupled Ocean/Atmosphere Mesoscale Prediction System (COAMPS);<sup>\*</sup> (1-km resolution) and Weather Research and Forecasting (WRF) mesoscale meteorological models (4-km resolution), as well as on climatological and satellite information, provided guidance for selecting IOPs for the campaign, whence all measurement systems were approved. This article reported an intriguing fog event observed on July 21, which was denoted by forecasters as IOP #9 (July 21, 1800 UTC–July 22, 1800 UTC). An excellent chance for fog with some mist was forecast, with background synoptic conditions having high pressure and a stable environment.

Fog indeed appeared on the afternoon of July 21. Detailed analysis of data of multiple instruments and video records showed convincingly that LLC appeared at some tens of meters aloft and disintegrated pieces (“cloud puffs”) descended to the surface to produce a fluctuating, and on average decreasing, field of near-ground visibility for about one and a half hours. Then the surface visibility dropped below 1 km for several hours, indicating fog. The near-surface averaged *RH* at the appearance of cloud puffs was ≈95%, indicating that their formation is not local, consistent with the notion of diffusing down of cloud puffs from a LLC. Even when the surface visibility first drops below 1 km (i.e., fog formation), the *RH* was less than 100%, indicating that *RH*-based fog predictions should be treated with circumspection for cases of fog appearance via top-down diffusion from LLC.

Scrutiny of campaign data led to a hypothesis for the case in point, as illustrated in Figure 13. Accordingly, during the evening transition, the MCBL is advected aloft over the heated IBL over Sable Island by southwesterly flow, generating an IL in between the two. The IL is initially weak in stability (as measured by a Richardson number), to the extent that turbulent eddies penetrate it and maintain communication and mixing between the two layers. During the day, the atmosphere over the ocean and land is clear of fog and clouds but with high *RH* ~ 90% in the MCBL and IBL, as evident from satellite images (Figure S2

in the Supplementary Material). As the evening transition progresses with differential temperature evolution in the IBL and MCBL, the stratification (stability) of the IL strengthens to cut off communication between the IBL and MCBL, with eddies flattening at the interface rather than penetrating it. Slow local mixing within the IL via local instabilities may cause mixing between air from the IBL and MCBL to saturate the IL through the Taylor mixing mechanism (Taylor, 1917), leading to a LLC within the IL, in much the same way as the local mixing in an IL discussed in (Strang & Fernando, 2001). Slow entrainment at the bottom of the LLC (or IL) by IBL turbulence generates descending “puffs” of saturated air, leading first to fluctuating visibility because of randomly moving puffs of saturated air parcels; as more puffs populate the cooling IBL, a saturated air layer is generated with visibility  $< 1 \text{ km}$  (fog) appearing.

It is instructive to discuss the profiles of Figure 9 in view of the mechanisms in Figure 13. The hypothesis was that in the early afternoon there will be an IL but eddies still penetrate the entire depth  $h_b$  of the land CBL (LCBL) to maintain active turbulence, whereas later in the evening transition the MCBL turbulence collapses to separate an actively turbulent IBL (driven mainly by shear) from the weakly turbulent advected MCBL aloft by the IL. The former is only possible if turbulent eddies from the IBL penetrate the stable IL and communicate with the overlying MCBL during the day. The requirement for such an actively turbulent IL with penetrating eddies from below has been discussed in many earlier works (see the review in Gregg (1987)), for which the condition involves a bulk Richardson number:  $\Delta b L_u / \sigma^2 < Ri_{\text{cr}}$ , where  $\Delta b$  is the buoyancy jump across the IL,  $L_u$  and  $\sigma$ , respectively, are the integral length-scale and characteristic rms velocity of penetrating turbulence, and  $Ri_{\text{cr}}$  is a critical Richardson number  $Ri_{\text{cr}} \approx \mathcal{O}(1)$ . Recent estimates show  $Ri_{\text{cr}} = 1.5$  in this setting (Fernando et al., 2023).

Based on the profiles at 1800 UTC,  $\Delta b = 0.047 \text{ m}\cdot\text{s}^{-2}$ ,  $L_u \approx 0.25h_l$  (Hunt, 1984),  $h_l \approx 30 \text{ m}$ ,  $\sigma = 0.62 \text{ m}\cdot\text{s}^{-1}$ . It is possible to evaluate  $\Delta b L_u / \sigma^2 = 0.92 < Ri_{\text{cr}}$ , which is an interface porous to turbulent eddies. On the other hand, the conditions for the 2100 UTC soundings are different, where the collapse of the MCBL has already started and, according to Figure 13b, where eddies of the two layers are separated by a stronger IL that inhibits turbulent transport between the layers. In this case, if this vertical profile is considered with turbulence statistics at 2120 UTC (after the turbulence spikes at 2100, seen in Figure 11c),  $\Delta b = 0.058 \text{ m}\cdot\text{s}^{-2}$ ,  $L_u \approx 0.25h_l$ ,  $h_l \approx 30 \text{ m}$ ,  $\sigma = 0.32 \text{ m}\cdot\text{s}^{-1}$ ,  $\Delta b L_u / \sigma^2 = 4.30 > Ri_{\text{cr}}$ , indicating a lack of direct communication between MCBL and IBL from 2120 UTC onwards. As such, the MCBL is devoid of a TKE generating mechanism, as shear therein is weak, thus leading to turbulent

collapse. The IBL is still undergoing shear production (but weaker buoyant production) near the ground, and hence within the IL the LLC can be entrained and diffused down to the surface in the form of fog.

During the evening transition, before the collapse of turbulence in the upper layer and formation of an IL sufficiently strong to decouple the IBL and MCBL at 2035 UTC (Table 2), the turbulent eddies were hypothesized to penetrate between the two layers and carry a heat flux to the upper layer, but with time the TKE of the eddies decreases and becomes devoid of a buoyancy contribution at 2200 UTC. Thereafter the IBL turbulence is dominated by shear, but weaker and confined to a layer of IBL of depth  $h_L$ .

Of the 14 IOPs conducted during Fatima–GB, this is the only event where locally forming LLC stratus was involved in fog genesis, and hence can be compared with a conventional slow LLC base-lowering mechanism as a result of subsidence. It was found that fog was generated by rapid descent of cloud puffs resulting from entrainment from the cloud base to the surface, rather than gradual lowering of the cloud base. Puffs first led to fluctuating visibility and then to fog upon sufficient accumulation of puffs in the surface layer. Therefore, entrainment from stratus base is a mechanism that should be accurately parameterized in Numerical Weather Prediction (NWP) models if the mechanism proposed above is to be captured. (Fernando et al., 2021) noted that a super (persistent, dense) fog event was missed by the NWP model COAMPS® because of inaccurate cloud-base entrainment parameterizations, and the present work supports this notion. The present work, in addition, proposes a mechanism of LLC formation over islands in a stable interfacial layer (IL) between the internal boundary layer and marine convective boundary layer during the evening transition. Capturing IL in NWP is also difficult, as the processes involved are governed by stratified flow dynamics, representation of which in NWP remains a challenge. Improved dynamic/thermodynamic parameterizations with stable, unstable, and transitional stratified turbulence of the atmospheric surface layer will be an edifying topic for future fog research. Simulations of IOP-9 using COAMPS® and WRF models are afoot, including studies of the ability of these models to elicit the processes hypothesized in Section 5. The results will appear in future publications.

## ACKNOWLEDGEMENTS

The authors thank Alexei Perelet, Reno Sit, Jay Orson Hyde, Ronald Scott Coppersmith, Ryan Yamaguchi, Alexis Trottier-Paquet, and Evan Newman for their contributions to data acquisition efforts during the Fatima Sable Island field campaign. The authors also thank Paul Leblanc, Marvin Willis, Jason Surette, and the entire Parks Canada

Sable Island team for their logistical contributions to field operations.

## FUNDING INFORMATION

The work was supported by Grant N00014-21-1-2296 (Fatima Multidisciplinary University Research Initiative) of the Office of Naval Research, administered by the Marine Meteorology and Space Program.

## CONFLICT OF INTEREST STATEMENT

The authors declare no conflict of interest.

## DATA AVAILABILITY STATEMENT

Data are available on request from the authors.

## ENDNOTE

<sup>1</sup>This article can be found online at <https://www.nber.org/papers/w26541>.

## ORCID

Thomas J. Hintz  <https://orcid.org/0009-0006-4059-2858>  
 Stef L. Bardoel  <https://orcid.org/0009-0002-5563-285X>  
 Saša Gaberšek  <https://orcid.org/0000-0002-2287-8776>

## REFERENCES

- Bardoel, S.L., Horna Muñoz, D.V., Grachev, A.A., Krishnamurthy, R., Chamorro, L.P. & Fernando, H.J. (2021) Fog formation related to gravity currents interacting with coastal topography. *Boundary-Layer Meteorology*, 181(2-3), 499–521.
- Barwick, P.J., Li, S., Lin, L. & Zou, E. (2019) From fog to smog: The value of pollution information. <https://www.nber.org/papers/w26541>
- Blay-Carreras, E., Pardyjak, E., Pino, D., Hoch, S., Cuxart, J., Martínez, D. et al. (2015) Lifted temperature minimum during the atmospheric evening transition. *Atmospheric Chemistry and Physics*, 15(12), 6981–6991.
- Byers, H., Landsberg, H., Wexler, H., Haurwitz, B., Spilhaus, A., Willett, H. et al. (1951) Fog. In: *Compendium of Meteorology: Prepared under the Direction of the Committee on the Compendium of Meteorology*, Boston, MA: American Meteorological Society; pp. 1179–1189.
- Caughey, S. & Kaimal, J. (1977) Vertical heat flux in the convective boundary layer. *Quarterly Journal of the Royal Meteorological Society*, 103(438), 811–815.
- Caughey, S. & Palmer, S. (1979) Some aspects of turbulence structure through the depth of the convective boundary layer. *Quarterly Journal of the Royal Meteorological Society*, 105(446), 811–827.
- Dorman, C.E., Mejia, J., Koračin, D. & McEvoy, D. (2017) *Worldwide Marine Fog Occurrence and Climatology*. New York, NY: Springer.
- Duynderke, P.G. (1991) Radiation fog: A comparison of model simulation with detailed observations. *Monthly Weather Review*, 119(2), 324–341.
- Fernando, H. & Hunt, J. (1997) Turbulence, waves and mixing at shear-free density interfaces. Part 1. A theoretical model. *Journal of Fluid Mechanics*, 347, 197–234.
- Fernando, H.J. (1988) The growth of a turbulent patch in a stratified fluid. *Journal of Fluid Mechanics*, 190, 55–70.
- Fernando, H.J., Gultepe, I., Dorman, C., Pardyjak, E., Wang, Q., Hoch, S. et al. (2021) C-FOG: life of coastal fog. *Bulletin of the American Meteorological Society*, 102(2), E244–E272.
- Fernando, H.J.S. (1991) Turbulent mixing in stratified fluids. *Annual Review of Fluid Mechanics*, 23(1), 455–493.
- Fernando, H.J.S., Wang, S., Huang, K.Y. & Creegan, E. (2023) Fog-laden density staircases in the marine atmospheric boundary layer. *Environmental Fluid Mechanics*, 23, 489–510.
- Fernando, H.J.S., Richter, D., Coppersmith, R.S., Huang, K., Dowling, A., Hintz, T. et al. (2024) Fatima-GB: Searching clarity within Marine Fog. *Bulletin of the American Meteorological Society*.
- Fiorino, S.T., Bose-Pillai, S.R., Schmidt, J., Elmore, B. & Keefer, K. (2020) Implications of four-dimensional weather cubes for improved cloud-free line-of-sight assessments of free-space optical communications link performance. *Optical Engineering*, 59(8), 081808-1–081808-18.
- Fitzjarrald, D. & Lala, G. (1989) Hudson valley fog experiments. *Journal of Applied Meteorology and Climatology*, 28(12), 1303–1328.
- Goldshmid, R.H., Winiarska, E. & Liberzon, D. (2022) Next generation combined sonic-hotfilm anemometer: wind alignment and automated calibration procedure using deep learning. *Experiments in Fluids*, 63(1), 30.
- Gregg, M. (1987) Diapycnal mixing in the thermocline: A review. *Journal of Geophysical Research: Oceans*, 92(C5), 5249–5286.
- Gultepe, I., Milbrandt, J.A. & Zhou, B. (2017) Marine fog: A review on microphysics and visibility prediction. In: *Marine fog: Challenges and Advancements in Observations, Modeling, and Forecasting*. New York, NY: Springer Atmospheric Sciences; pp. 345–394.
- Gultepe, I., Tardif, R., Michaelides, S.C., Cermak, J., Bott, A., Bendix, J. et al. (2007) Fog research: A review of past achievements and future perspectives. *Pure and Applied Geophysics*, 164, 1121–1159.
- Gultepe, I., Zhou, B., Milbrandt, J., Bott, A., Li, Y., Heymsfield, A.J. et al. (2015) A review on ice fog measurements and modeling. *Atmospheric Research*, 151, 2–19.
- Hanna, S.R. (1969) The thickness of the planetary boundary layer. *Atmospheric Environment* (1967), 3(5), 519–536.
- Hannoun, I.A. (1987) *Turbulent mixing in stably-stratified fluids subjected to zero-mean shear*. PhD thesis. Pasadena, CA: California Institute of Technology. <https://thesis.library.caltech.edu/854/>
- Hunt, J. (1984) Turbulence structure in thermal convection and shear-free boundary layers. *Journal of Fluid Mechanics*, 138, 161–184.
- Johnson, G. & Graschel, J. (1992) *Sea Fog and Stratus: A Major Aviation and Marine Hazard in the Northern Gulf of Mexico*. Washington, D.C: National Oceanic and Atmospheric Administration. [https://repository.library.noaa.gov/view/noaa/6349/noaa\\_6349\\_DS1.pdf](https://repository.library.noaa.gov/view/noaa/6349/noaa_6349_DS1.pdf)
- Kaimal, J., Wyngaard, J., Haugen, D., Coté, O., Izumi, Y., Caughey, S. et al. (1976) Turbulence structure in the convective boundary layer. *Journal of the Atmospheric Sciences*, 33(11), 2152–2169.
- Kaymak, Y., Rojas-Cessa, R., Feng, J., Ansary, N., Zhou, M. & Zhang, T. (2018) A survey on acquisition, tracking, and pointing mechanisms for mobile free-space optical communications. *IEEE Communications & Tutorials*, 20(2), 1104–1123.
- Kit, E., Cherkassky, A., Sant, T. & Fernando, H.J.S. (2010) In situ calibration of hot-film probes using a collocated sonic anemometer:

- Implementation of a neural network. *Journal of Atmospheric and Oceanic Technology*, 27(1), 23–41.
- Klemm, O., Schemenauer, R.S., Lummerich, A., Cereceda, P., Marzol, V., Corell, D. et al. (2012) Fog as a fresh-water resource: overview and perspectives. *Ambio*, 41(3), 221–234.
- Koračin, D. & Dorman, C.E. (2017) *Marine fog: Challenges and Advancements in Observations, Modeling, and Forecasting*. New York, NY: Springer.
- Koračin, D., Dorman, C.E., Lewis, J.M., Hudson, J.G., Wilcox, E.M. & Torregrosa, A. (2014) Marine fog: A review. *Atmospheric Research*, 143, 142–175.
- Large, W. & Pond, S. (1982) Sensible and latent heat flux measurements over the ocean. *Journal of Physical Oceanography*, 12(5), 464–482.
- Lothon, M., Lohou, F., Pino, D., Couvreux, F., Pardyjak, E., Reuder, J. et al. (2014) The BLLAST field experiment: Boundary-layer late afternoon and sunset turbulence. *Atmospheric Chemistry and Physics*, 14(20), 10931–10960.
- Maurer, M., Klemm, O., Lokys, H.L., Lin, N.H. et al. (2019) Trends of fog and visibility in Taiwan: climate change or air quality improvement? *Aerosol and Air Quality Research*, 19(4), 896–910.
- Mazon, J., Rojas, J., Lozano, M., Pino, D., Prats, X. & Miglietta, M. (2018) Influence of meteorological phenomena on worldwide aircraft accidents, 1967–2010. *Meteorological Applications*, 25(2), 236–245.
- Münkel, C. & Roininen, R. (2010) Unattended automatic monitoring of boundary layer structures with cost effective LIDAR ceilometers. *Geophysical Research Abstracts*, 12, 12.
- Nadeau, D., Pardyjak, E., Higgins, C., Fernando, H. & Parlange, M. (2011) A simple model for the afternoon and early evening decay of convective turbulence over different land surfaces. *Boundary-Layer Meteorology*, 141(2), 301–324.
- Pardyjak, E., Monti, P. & Fernando, H. (2002) Flux Richardson number measurements in stable atmospheric shear flows. *Journal of Fluid Mechanics*, 459, 307–316.
- Perram, G.P., Cusumano, S.J., Hengehold, R.L. & Fiorino, S.T. (2010) *An introduction to laser weapon systems*. Albuquerque, NM: Directed Energy Professional Society.
- Snowden, R.J., Stimpson, N. & Ruddle, R.A. (1998) Speed perception fogs up as visibility drops. *Nature*, 392(6675), 450.
- Strang, E. & Fernando, H. (2001) Entrainment and mixing in stratified shear flows. *Journal of Fluid Mechanics*, 428, 349–386.
- Tardif, R. & Rasmussen, R.M. (2007) Event-based climatology and typology of fog in the New York City region. *Journal of Applied Meteorology and Climatology*, 46(8), 1141–1168.
- Taylor, G. (1917) The formation of fog and mist. *Quarterly Journal of the Royal Meteorological Society*, 43(183), 241–268.
- Turton, J. & Brown, R. (1987) A comparison of a numerical model of radiation fog with detailed observations. *Quarterly Journal of the Royal Meteorological Society*, 113(475), 37–54.
- Wang, Q., Yamaguchi, R.T., Kalogiros, J.A., Daniels, Z., Alappattu, D.P., Jonsson, H. et al. (2021) Microphysics and optical attenuation in fog: Observations from two coastal sites. *Boundary-Layer Meteorology*, 181, 267–292.
- Weathers, K.C. (1999) The importance of cloud and fog in the maintenance of ecosystems. *Trends in Ecology & Evolution*, 14(6), 214–215.
- WMO. (2014) Aerodrome reports and forecasts: A users' handbook to the codes. *WMO-No752*, 1, 17–21.
- WMO. (2017) Guide to meteorological instruments and methods of observation. *WMO-No8*, 7, I.14-1–I.14-6.
- Woodcock, A.H. (1978) Marine fog droplets and salt nuclei—Part I. *Journal of Atmospheric Sciences*, 35(4), 657–664.

## SUPPORTING INFORMATION

Additional supporting information can be found online in the Supporting Information section at the end of this article.

**How to cite this article:** Hintz, T.J., Huang, K.Y., Hoch, S.W., Bardoe, S.L., Gaberšek, S., Gultepe, I. et al. (2024) A mechanism for coastal fog genesis at evening transition. *Quarterly Journal of the Royal Meteorological Society*, 1–17. Available from: <https://doi.org/10.1002/qj.4732>